Sheffield Hallam University

Tribological behaviour of Mo − W doped carbon-based coating at ambient condition

MANDAL, Paranjayee, EHIASARIAN, Arutiun <http://orcid.org/0000-0001-6080-3946> and HOVSEPIAN, Papken <http://orcid.org/0000-0002-1047-0407>

Citation:

Tribological behaviour of Mo − W doped carbon-based coating at ambient condition

Paranjayee Mandal*, Arutiun P. Ehiasarian and Papken Eh. Hovsepian

Nanotechnology Centre for PVD Research, HIPIMS Research Centre, Sheffield Hallam University, City Campus, Howard Street, Sheffield S1 1WB, United Kingdom

Email: 200712mum@gmail.com*, a.ehiasarian@shu.ac.uk, p.hovsepian@shu.ac.uk

Abstract

Poor adhesion strength and low thermal stability often restrict the tribological applications of the state-of-the-art diamond-like-carbon coatings in automotive industry. A novel carbon-based coating doped with molybdenum and tungsten (Mo−W−C) is deposited using the advantages of HIPIMS to overcome these limitations and to provide enhanced tribological performance. Low friction (μ=0.335 against steel counterpart) and high wear resistance (K_c=3.87×10^{-16} m^{3}N^{-1}m^{-1}) are observed after 7.5 km sliding distance and the coating remains intact within the wear track after sliding. It is concluded that the tribological performance of Mo−W−C coating at ambient condition excels due to its dense microstructure, interfacial adhesion strength and in-situ formation of solid lubricants such as graphitic carbon particles, MoO$_3$ and Magnéli phase oxides of molybdenum and tungsten in the transfer layer during sliding.

Keywords: Sliding friction, Third-body abrasion, Wear, Raman spectroscopy

1. Introduction

Diamond-like-carbon (DLC) coatings are extensively used as tribological coating in various automotive engine parts such as piston, piston rings, piston pins, gearbox and valve train components. DLC coatings provide high wear resistance ($K_c < 10^{-16}$ m^{3}N^{-1}m^{-1}) [1] along with a wide range of friction coefficient ($\mu = 0.05 - 1.0$ at ambient atmosphere and $\mu = 0.007 - 0.4$ under low pressure below 10^{-4} Pa) [1, 2] and hardness (10 – 80 GPa) [1 – 3] values. However, the commercial use of standard state-of-the-art DLC coating is compromised due to its poor adhesion strength (typically 30 – 40 N critical load) and low thermal stability up to ~350°C [4, 5]. Most of the state-of-the-art technologies utilise Argon ion etching as a surface pre-treatment method, which leads to amorphous interface and large amount of implanted gas in the interface. As a result, the adhesion strength decreases due to formation of porous and weak interface [6]. Moreover, the accumulation of high compressive residual stress (up to ~13 GPa) [2] during coating deposition further deteriorates the coating-substrate adhesion. Several approaches have been introduced to improve the adhesion strength of the DLC coating. As reported in the literature, Cr interlayer is introduced to decrease the compressive residual stress of the coating; therefore the adhesion strength is enhanced [7, 8]. Another approach to overcome the aspects of low adhesion and high compressive stress is to incorporate W into the DLC coating. The W – doping significantly reduces the internal residual stress of the coating, thus the coating-substrate adhesion is improved [7, 9, 10]. Moreover, the graded design in both coating's microstructure and composition significantly improve the coating-substrate adhesion. In order to resolve the second problem − poor thermal stability, metal elements such as Ti, Si, Cr, Mo or W are incorporated into the carbon-based coatings [4, 11, 12, 13]. These metal-doped DLC coatings improve the thermal stability and simultaneously reduce the friction coefficient compared to pure DLC coating [4, 10, 14 – 18]. Depending

on the doping element, coating microstructure and coating composition and the test conditions, the metal-doped DLC coatings provide a wide range of tribological properties.

Cr doped DLC and Cr doped graphitic carbon coatings provided an excellent combination of low wear coefficient ($10^{-16} - 10^{-18}$ $m^3N^{-1}m^{-1}$) and a wide range of friction coefficient (0.06 − 0.4) during dry sliding depending on the test parameters [1, 17, 19 − 25]. In water and oil lubricated conditions, the friction coefficient of these coatings ranged from 0.1 to 0.33 [26] and from 0.05 to 0.15 [27] respectively and the values of the wear coefficient were found as $\sim10^{-15} - 10^{-16}$ $m^3N^{-1}m^{-1}$ for both [26, 27]. Improvement in the friction behaviour ($\mu = 0.05 - 0.2$) was reported for Si-DLC coatings in a wide range of environmental condition including humid air [14, 18]. Similar development was found for Ti-DLC films during dry sliding ($\mu = 0.01 - 0.2$) [28 − 30]. Mo-DLC film having 11% Mo content showed a friction coefficient of <0.1 and improved wear resistance [15]. Almost similar friction and wear behaviour ($\mu=0.09 - 0.12$ and $K_c \sim10^{-15} - 10^{-16}$ $m^3N^{-1}m^{-1}$) was reported for W-DLC films [10]. In the contrary, other studies documented very high friction coefficient of W-DLC coating (up to 0.4) at ambient condition [7, 31] and reduction in friction coefficient was observed at high temperature ($\mu \leq 0.25$ in the range of 400°C − 500°C) due to formation of tungsten oxide [31].

It is important to note that the rise in temperature greatly influences the friction behaviour of metal-doped DLC coatings. The performance degrades at high temperature due to graphitisation of the carbon-based coatings. Thus the tribological behaviour in high temperature is benefitted when metal-dopant increases the thermal stability of the coating. The thermal stability of the Cr and Si doped DLC coatings was reported in the range of 300°C − 400°C [12, 32] and 300°C − 500°C [11, 14] respectively depending on the

coating deposition procedure and test conditions. The oxidation resistance of Ti-doped DLC coating was reported up to ~450°C [4] whereas Mo-DLC and W-DLC coatings were found thermally stable up to ~500°C [13]. In brief, Si, Mo or W improve the thermal stability of DLC coatings compared to other dopants, however the tribological properties are more significantly enhanced when Mo or W is used as a dopant in place of Si. This encourages the idea of synergizing combined benefits of Mo-DLC and W-DLC coatings by producing a carbon-based coating doped with Mo and W atoms simultaneously, which has been adopted in the present work.

The coating deposition process defines the coating microstructure as well as the adhesion strength. A good tribological performance (i.e. low friction and high wear resistance) can be achieved when coatings show dense microstructure and strong coating-substrate adhesion. Strong adhesion prevents the coating delamination whereas the dense coating microstructure helps to withstand the wear during sliding. The High Power Impulse Magnetron Sputtering (HIPIMS) is a renowned technique that fulfils these criteria [6, 33, 34]. Most of the sputtering processes suffer from occurrence of arc during film deposition, but the use of short pulses in HIPIMS technology results in almost stable and arc-free deposition. Moreover, this technology provides high ionisation degree of the plasma particles, which leads to better adhesion and less lattice defects compared to other PVD techniques such as magnetron sputtering. In the present study, the authors investigate the tribological properties at ambient condition and discuss the friction and wear mechanism of the novel Mo − W doped carbon-based coating (Mo−W−C) deposited by new technology utilising the merits of High Power Impulse Magnetron Sputtering (HIPIMS).

2. Experimental details

2.1. Sample preparation and coating deposition

Prior to the coating deposition, the M2 grade HSS and 304 SS disc samples were mirror polished (average R_a ~0.01 μm) with 6 μm and 1 μm diamond pastes. The polished samples and the Si wafers were cleaned in an industrial sized automated ultrasonic cleaning line to remove surface impurities and then dried in a vacuum drier before loading into the coating chamber. The Mo−W−C coating was deposited using HIPIMS + UBM techniques in an industrial sized Hauzer HTC 1000−4 PVD coating machine enabled with HIPIMS technology at Sheffield Hallam University. Three graphite targets were operated in UBM mode and a compound target containing both Mo and W was operated with HIPIMS mode during coating deposition. All the samples experienced three-fold rotation in order to achieve homogeneity in the direction of coating growth. Prior to the coating deposition, the targets were sputter-cleaned and the sample surfaces were further pre-treated by HIPIMS ion etching (using both Mo and W) [6]. A base layer was deposited in reactive Ar + N_2 atmosphere in order to enhance the coating − substrate adhesion, which was followed by the deposition of the Mo−W−C coating in Ar atmosphere. Thus the coating architecture is consisted of a HIPIMS treated interface, Mo − W − N base layer and a Mo − W − C layer on the top. The coated HSS and SS disc samples were submitted to different evaluation tests including adhesion, hardness, pin-on-disc and structural characterisations and the coated Si wafers were used for coating thickness and surface roughness measurements.

2.2. Characterisation techniques

2.2.1. Scanning electron microscopy (SEM)

FEI NOVA NANOSEM 200 coupled with Energy Dispersive X-ray (EDX) analysis module (Oxford instruments X-max detector with INCA analysis software) was used for studying microstructural and tribological properties of the Mo−W−C coating. The secondary electron detector and the thermoluminiscence detector were used for the topographical imaging and measurement of the coating thickness respectively. The X-ray mapping was done on the fractured cross-section of the coated sample and on the wear scar of the counterpart in order to identify the distribution of elements along the coating thickness and on the wear scar of the counterpart respectively.

2.2.2. X-ray diffraction (XRD)

The XRD study was carried out for microstructural characterisation of the as-deposited coating using a PANalytical Empyrean PIXcel 3D automated diffractometer. The microstructure and the phase composition of the as-deposited coated surface were determined using Bragg-Brentano (B − B) and glancing angle geometry (GAXRD). The continuous scanning was done from $2\theta = 20° − 130°$ with a step size of $0.026°$ for Bragg-Brentano geometry. The scanning range for glancing angle geometry was selected as $2\theta = 20° − 120°$ with an incident angle of $2°$. The Miller indices for all the phases present in the XRD patterns were calculated and shown in the respective figures. The X-ray source was Cu−Kα radiation with a wavelength of 1.54 nm and the voltage and current of X-ray generation tube was 45 kV and 40 mA respectively.

2.2.3. Scratch test

An automatic scratch tester REVETEST developed by CSM instruments was used to evaluate the critical load (L_c) for coating delamination, which measured the adhesion strength of the coating. The scratch tester was equipped with a cone shaped (120°) Rockwell type diamond indenter, which was allowed to scratch 10 mm length on the coated HSS disc. A pre-set load of 10 N was used at the start of scratching. The normal load was gradually increased with the forward movement of the indenter and the finishing load was fixed at 100 N. The scratch track and the magnitude of critical load (L_c) were determined with the help of an optical microscope, attached to the scratch tester.

2.2.4. Nanoindentation

The nanohardness and the elastic modulus of the as-deposited coating were measured using the CSM nanoindentation tester. The Berkovich diamond indenter was driven normal to the coated sample surface by applying load up to a pre-set value and then the load was gradually retracted until partial or complete relaxation of the material. To avoid substrate contribution during hardness measurement, the indentation depth should be <10% of the total coating thickness. A pre-set load of 10 mN was suitable for this purpose and indentations were repeated for 20 times to find out the average nanohardness. The nanohardness and the elastic modulus were calculated by the associated software using Oliver and Pharr method from the resultant load-displacement curves.

2.2.5. Pin-on-disc test

A CSM room temperature pin-on-disc tribometer was used to study the friction behaviour of the coatings at ambient conditions. The tribometer contained a rotating sample holder and a stationary ball was used as counterpart under the influence of a static load. In the

current study, the coated HSS disc sample was clamped to the rotating sample holder and the sliding was done against the uncoated 100Cr6 steel ball of 6 mm diameter. The static load and the sliding distance were fixed to 5 N and 7.5 km respectively for the experiment. This large sliding distance was selected to study the effect of metal dopants (Mo and W) on friction behaviour with time. The room temperature and the relative humidity recorded during the experiment were approximately 30°C and 30% respectively. The coefficient of friction $\mu = \dfrac{F_T}{F_N}$ was calculated during the experiment by the software using a measured value for the tangential force F_T and a normal force F_N exerted by a calibrated weight.

The wear coefficient was calculated using Archard's equation as $K_C = \dfrac{V}{F_N \times d}$ where V is the wear volume in m^3, F_N is the normal load in N and d is the sliding distance in meter. The volume of wear track (V) on the coated disc is calculated as $V = 2\pi RA$, where R is the wear track radius and A is the cross sectional area of the wear track. The wear track profile was scanned by the surface profilometer (DEKTAK 150) and the area of the scanned profile was calculated by the associated software. The scanning was repeated for 8 times on different sections of the wear track and their average was calculated. This average area A was used in the equation mentioned above. The wear coefficient of the uncoated steel ball was also calculated using the Archard's equation.

2.2.6. Raman spectroscopy

Raman spectroscopy was used to investigate the effect of metal dopants and to understand the wear mechanism during sliding. The Raman spectra were collected at random positions from the as-deposited coated surface, the wear track, the uncoated steel ball and

the transfer layer adhered to the counterpart surface after sliding using a Horiba-Jobin-Yvon LabRam HR800 integrated Raman spectrometer fitted with a green laser of wavelength 532 nm. A 10% transmission filter was used to reduce the intensity of the incident beam so that the damage due to irradiation could be avoided. The sample was exposed to the laser for 60 seconds for spectrum collection. The collected spectra were averaged over 5 acquisitions in the wavelength range of 50 – 2250 cm^{-1} for each test condition. However a single spectrum is collected from the wear debris adhered to the counterpart surface with a long exposure time of 240s to achieve a better signal-to-noise ratio. During analysis, the background of spectrum was corrected using a 2nd order polynomial whereas a multi-peak Gaussian-fitting function was used to deconvolute the spectrum and identify the Raman peaks. More details on choice of peak fitting function were described elsewhere [35].

3. Results and discussion

3.1. Characteristics of the as-deposited Mo-W-C coating

3.1.1. Coating microstructure and phase composition

Figure 1 shows the coating surface morphology and the fracture cross-section of the as-deposited Mo−W−C coating. The selected parameters during coating deposition provide dense columnar microstructure and a smooth surface with average surface roughness (R_a) in the order of 0.07 μm. The cross-sectional micrograph clearly reveals that the coating architecture consists of a thin Mo − W − N base layer (average thickness ~130 nm) adjacent to the Si substrate, which is followed by a thick (~2.2 μm) and dense columnar Mo − W − C layer on the top. The column diameter is observed ~170 nm with a flat top. The nucleation is via small grains and competitive growth that is resolved quickly to large

grains. At the same time, spherical grains with diameter of a few tens of nm are visible making the microstructure of typical of Zone II for PVD films according to the Thornton model. The column boundaries are clearly delineated.

The X-ray mapping is done on the fracture cross-section of the Mo−W−C coating to understand the elemental distribution across the coating thickness. Figure 2 demonstrates the elemental mapping showing the existence of C, Mo, W and N. Higher concentration of carbon is observed at the top coating layer compared to the dopant elements (Mo and W). Mo and W, which are uniformly distributed throughout the entire coating thickness, but their presence as expected is higher in the $Mo − W − N$ base layer.

Figure 3a shows the crystal structure of the as-deposited coating studied by XRD analysis using Bragg-Brentano geometry. The coating shows two peaks at ~35.8° and ~38°, whereas other peaks are from stainless steel substrate. The hexagonal WC [1 0 0] and WN [1 0 0] phases are present in the peak located at ~35.8° whereas the peak at ~38° is assigned to hexagonal W_2C [0 0 2] and Mo_2C [0 0 2] phases. Thus it is concluded that the top surface of the coating consists of metal carbide phases (WC, W_2C and Mo_2C) whereas the base layer contains metal nitride (WN) phases.

The microstructure and the phase composition of the as-deposited coated surface are further studied by GAXRD. Figure 3b shows the GAXRD pattern of the as-deposited coating. A single broad peak dominates the pattern indicating its nanocrystalline almost X-ray amorphous nature. The presence of hexagonal WC [1 0 0] phase at ~35.8° and hexagonal W_2C [0 0 2] and Mo_2C [0 0 2] phases at ~38° are detected within the broad peak. This confirms the findings of XRD pattern obtained through Bragg-Brentano

geometry (Fig. 3a). The morphology of the grains seen in the micrographs may be ascribed to a process of surface segregation of two phases during the growth of the film. The majority phase is carbon-rich and has an X-ray amorphous/nanocrystalline makeup as evidenced by the XRD patterns. A minority phase, probably metal-rich, may be segregated to column boundaries.

3.1.2.   Adhesion and hardness

The adhesion of the as-deposited coating is quantified by determining the critical load (L_c) at which adhesive failure is initiated due to the coating delamination. As shown in Fig. 4a, the coating withstands high critical loads (L_c) of up to 80.8 N after which the substrate is exposed due to adhesive failure. The adhesive failure is influenced by the coating thickness, structure as well as the hardness. Figure 4b shows the SEM image of the scratch track end at 100 N applied load. No flaking and interfacial spallation is observed inside and even beyond the scratch track end demonstrating excellent adhesion strength. This strong adhesion is attributed to the effective metal ion etching delivered by the HIPIMS technology [6]. The adhesion strength to the base layer may be due to the similar makeup of the base layer and coating that allows intensive linking between identical elements across the interface. This provides conditions of lower free energy on the surface i.e. more nucleation sites, which enhances the bonding strength between the two layers.

The average nanohardness and elastic modulus of the as-deposited coating are estimated from the characteristic loading-unloading curves and a typical loading-unloading curve is shown in Fig. 5. Absence of discrete steps in the loading curve indicates no fracture of the coating. At an applied load of 10 mN, the indentation depth at the end of loading period is

observed ~180 nm and the displacement during unloading is found ~100 nm. As the indentation depth is <1/10th of the total coating thickness, therefore this hysteresis loss is believed to be influenced by the dense columnar microstructure of the as-deposited coating. The average nanohardness of the as-deposited coating is observed in the range of ~1426 – 2090 HV with an average of ~1677.5 HV. The amorphous carbon matrix and the hard metal carbide phases present in the as-deposited coating simultaneously influence the coating hardness. Moreover the variation in hardness is probably observed due to the discontinuity of the mechanical properties between the column bodies and the column boundaries. The elastic modulus is found in the range of ~128 – 286 GPa with an average of 236.2 GPa.

3.2. Friction behaviour of Mo-W-C coating at ambient condition

The friction curve of Mo−W−C coating during dry sliding (against uncoated steel ball used as counterpart at 30°C temperature and at 30% relative humidity) is shown in Fig. 6. An average friction coefficient of ~ 0.417 is observed during initial run-in period of 200 m, which then decreases to ~0.333 throughout the steady-state period. Therefore the overall mean friction coefficient after a sliding distance of 7.5 km is evaluated as ~0.335. The friction curve is smooth during run-in period and initial steady-state period (up to ~1.5 km). However, oscillations are observed as the sliding progresses and the amplitude of oscillations is found mostly fluctuating towards the end of the test (after ~5.3 km). The oscillations of the friction coefficient are attributed to the formation of wear debris and a physisorbed layer of the water molecules on the surface leading to the stick-slip motion. It is widely published that the water molecules reduce the friction coefficient of carbon-based coatings by passivating the dangling bonds of the carbon [36]. In the presence of

wear debris however, the friction behaviour of the Mo−W−C coating is clearly influenced by both factors (moisture and debris) over the time. This is further evidenced by SEM and Raman analyses, which reveal that the friction coefficient is strongly influenced by the third-body abrasion during sliding. The effects of third-body abrasion and the moisture content on the friction behaviour are explained in following sections.

It should be noted that the amorphous carbon coatings provide very low friction coefficient (~0.05 − 0.15) at ambient condition, however it significantly fluctuates when the sliding distance is large enough (such as 7.5 km as chosen in this experiment). This point is established when the friction behaviour of a commercially available state-of-the-art amorphous multilayer DLC coating is observed under same test conditions. The ~3 μm thick DLC coating contains a thin Cr base layer, followed by a sputtered Cr−WC adhesion layer, a W:C−H intermediate layer and an a:C−H layer on the top. Thus this coating is defined as $DLC(Cr/Cr-WC/W:C-H/a:C-H)$ in Fig 6. During initial run-in period of 200 m, DLC coating shows an extremely low average friction coefficient of ~0.17, which is around 2.5 times higher than the friction coefficient of Mo−W−C coating. During steady-state period, the friction coefficient of DLC coating significantly increases in the range of ~0.25 − 0.4 leading to an average value of ~0.3, which is almost similar to the friction value obtained for Mo−W−C coating. At the end of sliding, the overall mean friction coefficient of DLC coating is found as ~0.297, which is close to the mean friction coefficient obtained for Mo−W−C coating.

a.   Third-body abrasive wear

Figure 7a shows the transfer layer formed on the ball surface after 7.5 km of sliding containing wear debris. The debris particles trapped inside the wear track during sliding,

experience severe plastic deformation and promote third-body abrasive wear. Closer analyses of this phenomena reveals that there are two types of debris: (a) loose debris particles, which continuously abrade against each other and the wear surfaces during sliding and (b) debris particles, which cold-weld to the counterpart surface during sliding and form a strongly bonded transfer layer (as shown in Fig. 7b). The friction coefficient is determined by the composition and the thickness of the transfer layer and the loose debris particles rolling in the wear track. X-ray mapping and Raman analyses show that the transfer layer is mainly composed of powder-like fine graphitic carbon particles and various metal oxides (discussed in section 3.3).

b.   *Effect of moisture content*

The humid test environment benefits the friction coefficient and determines the shape of the friction curve. As reported already, the water molecules are adsorbed on the coated surface during sliding and passivate the dangling bonds of the carbon at the sliding surface. The chemical inertness of the carbon atoms reduces the adhesive interactions between the sliding surfaces, which is manifested by the low values of the friction coefficient [36]. Further reduction in friction coefficient to ~0.335 is assisted by the graphitic carbon particles present in the transfer layer due to the carbon against carbon sliding mechanism.

This leads to the assumption that the wear debris act as a third-body sliding media in the tribological contact and define the friction behaviour during sliding. Therefore it can be speculated that the physical properties and more precisely the "internal friction" of this media determine the actual value of the coefficient of friction. This concept is similar to the concept of the role of the viscosity in liquids.

3.3. Wear of the Mo-W-C coating and the counterpart during dry sliding

3.3.1. Wear of the counterpart (uncoated 100Cr6 steel ball)

Figure 7b shows the wear scar on the counterpart, from which the wear coefficient of the counterpart calculated as $3.78 \times 10^{-18}\,m^3N^{-1}m^{-1}$, is found exceptionally low. The high wear resistance is attributed to the formation of transfer layer during sliding which promotes minimum wear on the counterpart surface. This behaviour is explained in details in the following section.

Figure 8 shows the X-ray mapping carried out on the wear scar of the counterpart surface after sliding. It is found that the adhered debris on the wear scar is composed of graphitic carbon particles, tungsten oxides and molybdenum oxides. The iron oxides generated from the counterpart during sliding, are accumulated mainly on the wear surface, which is free of adhered debris. The findings of the X-ray mapping are further supported by the Raman analyses as discussed below.

Figure 9a shows the Raman spectrum collected from the uncoated steel ball. A clear image of the ball is provided in the inset for convenience and the encircled area shows the position of spectrum collection. The spectrum is deconvoluted using Gaussian distribution into five peaks labelled as P1 − P5 in the spectrum range from approximately 50 − 1000 cm^{-1}. The centre and width of the peaks are provided in Table 1. All these peaks belong to the uncoated steel ball, which is further confirmed by the EDX spectrum (with major elements Fe and Cr) provided in the inset of Fig. 9a.

Figure 9b shows the Raman spectrum collected from the encircled area of the wear scar (image provided in the inset) on the counterpart surface, which is free of cold-welded wear

debris. The Gaussian distribution is used to deconvolute this spectrum and five peaks labelled as $P1^{/}$ – $P5^{/}$ are found in the spectrum range of ~50 – 1000 cm^{-1}. The centre and width of these peaks are listed in Table 1. Both the spectra collected from the uncoated ball and the wear scar (shown in Figs. 9a and 9b) have similar appearance, however a shift in the peak positions is observed after sliding. The uncoated steel ball reacts with the oxygen during sliding due to flash temperatures up to 800°C [37] generated at the asperity contacts. As a result, little amount of Fe_2O_3 and Cr_2O_3 are formed and accumulated on the wear scar. Therefore no significant change is observed in the spectrum shape however, the peaks are shifted indicating the oxidation of the steel ball after sliding. For example, the overlapping of Fe_2O_3 and Cr_2O_3 peaks significantly increases the width of peak P4 (in Fig. 9a) to ~311 cm^{-1} and shifts the centre of the peak to ~328 cm^{-1}. Thus, this peak is expressed in the spectrum as $P4^{/}$ [Fe_2O_3 + Cr_2O_3] in Fig. 9b. The dominant Raman peaks of Fe_2O_3 and Cr_2O_3 are reported in the literature at ~293 – 298 cm^{-1} [38] and ~300 cm^{-1} and ~350 cm^{-1} [39]. The EDX spectrum provided in the inset of Fig. 9b confirms the presence of Fe_2O_3 and Cr_2O_3 on the wear scar. It is believed that rest of the peaks are related to the steel ball and they do not contain any metal oxides. Based on the Raman analyses and the EDX spectrum, the possible chemical reactions are listed in equation set (1).

$$4Fe(counterpart) + 3O_2(air) \rightarrow 2Fe_2O_3$$
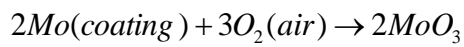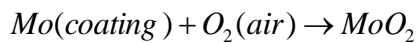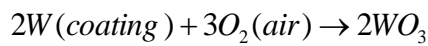$$4Cr(counterpart) + 3O_2(air) \rightarrow 2Cr_2O_3 \tag{1}$$

Figure 10 shows the Raman spectrum collected from the debris adhered to the counterpart surface after sliding (the debris is shown in the encircled area on the wear scar provided below the spectrum). The spectrum contains strong and distinct disordered (D) and sp^{2} bonded graphitic carbon (G) peaks along with different molybdenum and tungsten oxide

peaks. The wear debris generated from the coating contains molybdenum and tungsten carbide particles and free graphitic carbon particles. The metal carbides react with the oxygen during sliding due to high flash temperature at the asperity contacts and form different molybdenum and tungsten oxides via diffusion mechanism based on gradual replacement of carbon atoms by the ones of oxygen. These metal oxides and the free graphitic carbon particles are transformed to the counterpart surface during sliding forming a transfer layer. The EDX spectrum collected from the encircled area on the wear scar confirms the presence of metal oxides in the adhered debris.

The spectrum of the adhered debris contains two separate disordered graphitic peaks (D1 and D2) at 1172.91 cm^{-1} and 1392.64 cm^{-1} respectively, whereas the sp^2 bonded graphitic carbon peak (G) is found at 1591.40 cm^{-1}. The I_D/I_G ratio is calculated as 1.03. After deconvolution of the spectrum, a sharp peak appeared at the shoulder of the spectrum centred at ~335 cm^{-1} and having a width of ~215 cm^{-1}. This peak is formed due to overlapping of MoO_2, MoO_3 and WO_3 peaks; however some intermediate oxides of molybdenum and tungsten (Mo_4O_{11}, $W_{18}O_{49}$ and $W_{20}O_{58}$) can be present as well. The dominant Raman peaks of MoO_2 and MoO_3 are documented in the literature at ~357 cm^{-1} [40], and ~284 cm^{-1}, ~292 cm^{-1}, ~337 cm^{-1} and ~367 cm^{-1} [41] respectively. The leading peaks of WO_3 are reported at ~328 cm^{-1} [42], ~274 cm^{-1} and ~315 cm^{-1} [43]. The Raman peaks for Mo_4O_{11}, $W_{18}O_{49}$ and $W_{20}O_{58}$ are found at ~340 cm^{-1} [44], ~327 cm^{-1} [45], ~319 cm^{-1} and ~341 cm^{-1} [46] respectively. The spectrum contains a hump centred at ~929 cm^{-1} and having a peak width of ~108 cm^{-1}. This peak plausibly originates from the overlapping of several intermediate oxides of molybdenum such as Mo_4O_{11}, Mo_5O_{14} and Mo_8O_{23} formed during sliding. The dominant Raman peaks for Mo_4O_{11}, Mo_5O_{14} and Mo_8O_{23} are reported in the literature at ~907 cm^{-1}, ~902 cm^{-1}, ~902 cm^{-1} and ~958 cm^{-1} [47, 48 and

49] respectively. Furthermore, the peaks belonging to the steel ball (labelled as P1 − P3) are also observed in this spectrum. Table 2 lists the Raman peaks of the spectrum collected from the adhered debris. Based on the Raman analyses and the EDX spectrum, the possible chemical reactions are listed in equation set (2).

$$Principal \quad metal \quad oxides :$$
$$2W(coating) + 3O_2(air) \rightarrow 2WO_3$$
$$Mo(coating) + O_2(air) \rightarrow MoO_2$$
$$2Mo(coating) + 3O_2(air) \rightarrow 2MoO_3$$

$$Intermediate \quad metal \quad oxides :$$
$$36W(coating) + 49O_2(air) \rightarrow 2W_{18}O_{49}$$
$$20W(coating) + 29O_2(air) \rightarrow W_{20}O_{58}$$
$$8Mo(coating) + 11O_2(air) \rightarrow 2Mo_4O_{11}$$
$$5Mo(coating) + 7O_2(air) \rightarrow Mo_5O_{14}$$
$$16Mo(coating) + 23O_2(air) \rightarrow 2Mo_8O_{23} \tag{2}$$
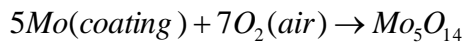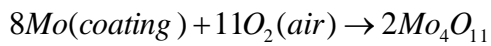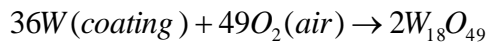
3.3.2. Wear of the Mo−W−C coating

Figure 11a shows the SEM image of a ~264 μm wide wear track on the Mo−W−C coating deposited on the HSS disc sample. The wear track is smooth and no grooves are observed inside the track. The transfer layer promotes minimum wear during sliding thus the value of wear coefficient is found as $3.87 \times 10^{-16} \, m^3 N^{-1} m^{-1}$. The coating remains intact within the wear track after the test as the EDX spectrum collected within the wear track is found same as that from the as-deposited surface. The absence of oxygen in the EDX spectrum indicates no adherence of metal oxides within the wear track. Furthermore, no accumulation of wear debris is observed even outside the wear track. This can be

attributed to the lower sticking probability due to cold welding phenomena of the debris to the surface of the coating material compared to the counterpart material.

Figure 11b illustrates the wear track profile after sliding. The depth of the wear track was measured with the help of software associated with the surface profilometer. The average depth of wear track is found as ~1.19 μm, which is less than the coating thickness of ~2.2 μm (Fig. 1b). This confirms that the coating is retained in the wear track after 7.5 km of sliding at ambient conditions. The enhanced wear performance of this coating is attributed to dense microstructure, strong interfacial adhesion and a high hardness value.

The Raman spectrum collected from the as-deposited surface is shown in Fig. 12a. After deconvolution of the spectrum, the distinct and dominant disordered (D) and sp^2 bonded graphitic carbon peaks (G) are observed. Their positions are found at 1387.04 cm^{-1} and 1574.32 cm^{-1} respectively and the I_D/I_G ratio is calculated as 1.96. The I_D/I_G ratio is an important parameter in Raman analysis to understand the bonding characteristics and to estimate the disorder in the carbon network. The I_D indicates the intensity of D peak due to the A_{1g} breathing mode of carbon atoms in six fold rings. D peak is active only in presence of disorder and therefore this mode is absent in perfect graphite. On the other hand, the I_G indicates the intensity of graphitic (G) peak resulting from the E_{2g} stretching motion for all pairs of sp^2 bonded carbon atoms [50, 51]. The as-deposited coating is graphitic, thus an increase in I_D/I_G ratio indicates an increase in disorder of carbon–carbon bonds in the coating after sliding [50].

Five peaks labelled as $P_a - P_e$ are observed after deconvolution of the spectrum of the as-deposited coating. The centre and the width of the peaks are listed in Table 3. Among

them, the peaks P_b and P_c (centred at ~342 cm^{-1} and ~652 cm^{-1} respectively) are found at two consecutive shoulders of the spectrum and corresponding peak widths are found as ~213 cm^{-1} and ~330 cm^{-1} respectively. These peaks are assigned to Mo$_2$C, because the dominant Raman peaks of Mo$_2$C are found in the literature at ~334 cm^{-1} and ~666 cm^{-1} [40]. The XRD analyses obtained through Bragg-Brentano (Fig. 3a) and glancing angle (Fig. 3b) geometry indicate that the as-deposited coating contains both molybdenum and tungsten carbide (Mo$_2$C, WC and W$_2$C) phases; however no tungsten carbides are detected in the Raman spectrum.

Figure 12b shows the Raman spectrum collected within the wear track after sliding. This spectrum has similar shape to that of the as-deposited coating (Fig. 12a). The EDX analysis indicates that no metal oxides are adhered to the bottom of the wear track and the coating remains intact after sliding (Fig. 11a). No debris is observed outside the wear track. On the other hand, the debris adhered to the counterpart surface contains tungsten and molybdenum oxides as indicated by the X-ray mapping and Raman analyses (Figs. 8 and 10). Therefore few metal oxide particles can possibly be present within the wear track, however their quantities are reasonably below the detection limit for EDX analysis. The Raman spectroscopy is employed to reveal the presence of metal oxides within the wear track.

After deconvolution of the spectrum collected within the wear track (Fig. 12b), two separate disordered peaks (D1 and D2) are found at 1109.65 cm^{-1} and 1382.04 cm^{-1} respectively, whereas the G peak is located at 1572.58 cm^{-1}. The I_D/I_G ratio is increased to 2.64 after sliding. It is speculated that the continuous rubbing action between the coating and the counterpart increases the disordering of bonds in the carbon network. The wear

debris is severely deformed during sliding and therefore the graphitic cluster size is reduced. This in turn increases the breathing mode of six fold rings leading to the development of D peak but does not affect the stretching motion of sp^2 bonded carbon atoms. Thus the I_D/I_G ratio is increased after sliding indicating an increase in disorder of carbon–carbon bonds.

It should be noted that the debris adhered to the counterpart surface shows lower degree of graphitisation (I_D/I_G ratio = 1.03) compared to the as-deposited coating (I_D/I_G ratio = 1.96) as well as the debris particles found in the wear track (I_D/I_G ratio = 2.64). As discussed, the as-deposited coating is graphitic and the debris particles originated from the coating are severely damaged during sliding and smeared all over the wear track. Thus the spectrum collected from the wear track shows an increased degree of graphitisation i.e. higher I_D/I_G ratio compared to the as-deposited coating. On the other hand, the spectrum collected from the debris adhered to the counterpart surface (Fig. 10) shows typical D and G peaks, which are similar to that observed in the amorphous carbon coating rather than the graphitic carbon coating. This indicates more disorder of the carbon−carbon bonds of the debris particles adhered to the counterpart surface rather than wear track. Because of this disorder, the graphitic cluster size is significantly decreased and the distortion of clusters eventually opens up the aromatic rings resulting in a decrease in D peak intensity. This does not affect the relative motion between sp^2 carbon bonds, thus G peak intensity remains same. Therefore, a significant decrease in I_D/I_G ratio is observed compared to the as-deposited coating indicating a possible transformation of nanocrystalline graphitic particles to amorphous phase due to severe plastic deformation during sliding [50].

The deconvoluted spectrum (collected from the wear track) in Fig. 12b shows three peaks labelled as $P_a^/ - P_c^/$ and a small peak centred at ~942 cm^{-1} in the spectrum range of ~50 – 1000 cm^{-1}. The centre and the width of the peaks are listed in Table 4. Fig. 12a shows that the as-deposited coating has two peaks (P_b and P_c) centred at ~342 cm^{-1} and ~652 cm^{-1} at two consecutive shoulders, which are slightly shifted to ~320 cm^{-1} and ~644 cm^{-1} after sliding (labelled as $P_b^/ - P_c^/$) as indicated in Fig. 12b. The corresponding peak widths are found as ~226 cm^{-1} and ~383 cm^{-1} respectively. The phases from as-deposited coating are still present within the wear track; however it is believed, that the formation of new compounds after sliding results in shifting of peak position and in increase of the corresponding peak width. The Mo_2C phase from the as-deposited coating is retained in the peaks centred at ~320 cm^{-1} and ~644 cm^{-1} however these peaks are further influenced by the formation of metal oxides. The leading Raman peaks of WO_3 are found at ~315 cm^{-1} [43] and ~328 cm^{-1} [42] whereas the intermediate oxides of tungsten such as $W_{18}O_{49}$ and $W_{20}O_{58}$ shows dominant Raman peak position at ~327 cm^{-1} corresponding to the one found in [45] and ~319 cm^{-1} and ~341 cm^{-1} corresponding to the reference [46]. Thus peak $P_b^/$ centred at ~320 cm^{-1} is possibly formed due to overlapping of Mo_2C, WO_3, $W_{18}O_{49}$ and $W_{20}O_{58}$ and is expressed in the spectrum as $Mo_2C[W_xO_y]$, where W_xO_y indicates the WO_3, $W_{18}O_{49}$ and $W_{20}O_{58}$ peaks altogether. Similarly, the leading Raman peaks of MoO_2 and MoO_3 are found at ~640 cm^{-1} and ~666 cm^{-1} corresponding to the reference [40] and at ~667 cm^{-1} corresponding to the reference [41], whereas intermediate molybdenum oxide Mo_8O_{23} has a dominant Raman peak at ~658 cm^{-1} [49]. Therefore peak $P_c^/$ centred at ~644 cm^{-1} is plausibly formed due to overlapping of Mo_2C, MoO_2, MoO_3 and Mo_8O_{23} and is expressed in the spectrum as $Mo_2C[Mo_xO_y]$, where Mo_xO_y indicates the MoO_2, MoO_3 and Mo_8O_{23} peaks altogether. Another small peak centred at ~942 cm^{-1} and having a peak

width of ~150 cm^{-1} appears in the spectrum probably indicating the presence of WC phase as the leading Raman peak of WC is reported in the literature at ~960 cm^{-1} [52].

3.4. Influence of the wear products on the tribological behaviour

The friction and wear behaviour during dry sliding is simultaneously influenced by the powder-like graphitic carbon particles and the metal oxide particles (different principal and intermediate oxides of tungsten and molybdenum, iron oxides and chromium oxides) present in the transfer layer. Raman analyses of the counterpart and the coating (sections 3.3.1 and 3.3.2) reveal the wear mechanism during dry sliding.

The wear debris generated during sliding contains tungsten carbide, molybdenum carbide and free graphitic carbon particles from coating and particles from the uncoated steel ball. As reported, the flash temperature at the asperity contacts reaches up to 800°C [37] during sliding, which promotes the chemical reactions between the wear debris and the oxygen from the environment. As a result, different metal oxides are formed within the wear track and transformed to the counterpart surface during sliding. Raman analyses indicate the presence of WO_3 and intermediate tungsten oxides ($W_{18}O_{49}$ and $W_{20}O_{58}$), MoO_3, MoO_2 and intermediate molybdenum oxides (Mo_4O_{11} and Mo_5O_{14} and Mo_8O_{23}) and iron and chromium oxides (Fe_2O_3 and Cr_2O_3) in the transfer layer. These metal oxides have stronger chemical affinity towards steel rather than the coating has, therefore they are strongly adhering to the ball surface (as shown in Fig. 7b). It can be concluded that the wear mechanism during dry sliding is *oxidative* and the relevant chemical reactions have been listed in equation sets (1) and (2).

It is well known that WO_3 consists of a three-dimensional array of corner-linked WO_6 octahedra, MoO_2 has a distorted rutile structure consisting of edge-shared MoO_6 octahedra and both the Fe_2O_3 and Cr_2O_3 have their structure similar to that of corundum crystallites. None of these structures promotes sliding. On the other hand, MoO_3 is composed of distorted MoO_6 octahedra, which forms chains by sharing the edges. The chains are cross-linked by oxygen atoms and form a layered structure. Therefore MoO_3 acts effectively as a solid lubricant unlike other oxides and promotes sliding at ambient conditions. The oxidation of tungsten and molybdenum carbide debris particles during sliding form *MeO$_3$* structures (where *Me* corresponds to = W, Mo) consisting of corner-shared *MeO$_6$* octahedra. The heat generated at the asperity contacts promotes chemical reactions between these metal oxides and the powdered metal present in the transfer layer. The reduction of *MeO$_3$* compound results in different intermediate oxides unless *MeO$_2$* structures (WO_2 and MoO_2) containing edge-shared *MeO$_6$* octahedra are formed. In between the *MeO$_3$* and *MeO$_2$* structures, a series of intermediate oxides with a stoichiometry of *Me$_n$O$_{3n-1}$* may form and they are known as Magnéli phase oxides. These oxides contain slabs of corner-shared octahedra and share edges with the octahedra of the identical adjacent slabs. These slabs promote the crystallographic shear [53].

The different metal oxides generated from Mo−W−C coating due to the ***oxidative*** wear mechanism play an important role in reduction of the friction coefficient at ambient conditions. Among the various metal oxides formed during sliding, most beneficial are the molybdenum trioxide (MoO_3) and the Magnéli phase oxides which act as the solid lubricants due to their unique layered structure and therefore promote sliding and reduce the coefficient of friction. The sliding is further benefitted by the presence of graphitic carbon particles in the transfer layer. Altogether these solid lubricants (graphitic carbon

particles, MoO_3 and the Magnéli phase oxides) reduce the average friction coefficient value to ~0.335 at ambient conditions and as a result, the wear is significantly minimised.

4. Conclusions

The mechanical and tribological properties of the Mo−W−C coating are investigated at ambient conditions (~30°C and at 30% relative humidity). The conclusions derived from this study are summarised as follows:

- The fracture cross-section of the coating shows dense columnar microstructure. The GAXRD analyses indicate a nanocrystalline almost amorphous structure and the presence of hard tungsten and molybdenum carbide phases.

- The HIPIMS etching is useful to achieve a strong interfacial adhesion (L_c ~80.8 N and no spallation was observed up to 100 N load) whereas the coating microstructure results in relatively high hardness value of ~1677.5 HV at 10 mN load.

- The average friction coefficient is found to be ~0.335. The friction behaviour during sliding is strongly influenced by the third-body abrasive wear and the humid test environment. At these conditions, a transfer layer is formed, which is composed of fine graphitic carbon particles and different metal oxides.

- Raman analyses show that the as-deposited coating has an amorphous matrix reinforced with tungsten and molybdenum carbides and free carbon particles. For as-

deposited coating, the I_D/I_G ratio is found to be 1.96. After sliding this value increases to 2.64 indicating a greater disorder of carbon−carbon bonds in the carbon network.

- The surface analyses employed in this research reveal that at ambient condition the wear mechanism of the Mo−W−C coating is *oxidative*. It has been found that the transferred layer consists of two types of oxides, namely principal metal oxides (WO_3, MoO_2, MoO_3, Fe_2O_3 and Cr_2O_3) and Magnéli phase oxides (Mo_4O_{11}, Mo_5O_{14}, Mo_8O_{23}, $W_{18}O_{49}$ and $W_{20}O_{58}$).

- The MoO_3 and the Magnéli phase oxides act as solid lubricants due to their layered structure which is similar to that of the graphitic carbon particles present in the transfer layer. As a result, the values of wear coefficients of the coating and the counterpart are found as low as 3.87×10^{-16} $m^3N^{-1}m^{-1}$ and 3.78×10^{-18} $m^3N^{-1}m^{-1}$ respectively. This confirms an excellent wear resistance of the Mo−W−C coating at ambient conditions.

Reference:

[1] Yang, S., Camino, D., Jones, A.H.S., Teer, D.G. Deposition and tribological behaviour of sputtered carbon hard coatings. Surface and Coatings Technology. 2000; 124: 110–116

[2] Grill, A. Diamond-like carbon: state of the art. Diamond and Related Materials. 1999; 8: 428–434

[3] Walter, K.C., Kung, H., Levine, T., Tesmer, J.T., Kodali, P., Wood, B.P., Rej, D.J., Nastasi, M., Koskinen, J., Hirvonen, J. P. Characterization and performance of diamond-like carbon films synthesized by plasma- and ion-beam-based techniques. Surface and Coatings Technology. 1995; 74–75: 734–738

[4] Ma, G., Gong, S., Lin, G., Zhang, L., Sun, G. A study of structure and properties of Ti-doped DLC film by reactive magnetron sputtering with ion implantation. Applied Surface Science. 2012; 258: 3045–3050

[5] Wang, D. Y., Chang, C. L., Ho, W. Y. Oxidation behaviour of diamond-like carbon films. Surface and Coatings Technology. 1999; 120–121: 138–144

[6] Ehiasarian A.P., Wen J. G., and Petrov I. Interface microstructure engineering by high power impulse magnetron sputtering for the enhancement of adhesion, J. Appl. Phys. 2007; 101: 054301

[7] Wanstrand, O., Larsson, M., Hedenqvist, P. Mechanical and tribological evaluation of PVD WC/C coatings. Surface and Coatings Technology. 1999; 111: 247–254

[8] Jeon Y., Park y. S., Kim H. J. and Hong B. Tribological Properties of Ultrathin DLC Films with and without Metal Interlayers. Journal of the Korean Physical Society. 2007; 51 (3): 1124 – 1128

[9] Corbella, C., Oncins, G., Gomez, M.A., Polo, M.C., Pascual, E., Garcia-Ce´spedes, J., Andujar, J.L., Bertran, E. Structure of diamond-like carbon films containing transition metals deposited by reactive magnetron sputtering. Diamond & Related Materials. 2005; 14: 1103–1107

[10] Silva, C.W.M., Branco, J. R.T., Cavaleiro A. How can H content influence the tribological behaviour of W-containing DLC coatings. Solid State Sciences. 2009; 11: 1778–1782

[11] Wu W. J., Hon, M. H. Thermal stability of diamond-like carbon films with added silicon. Surface and Coatings Technology. 1999; 111: 134–140

[12] Chiu, M.C., Hsieh W.P., Ho W.Y., Wang D. Y., Shieu, F.S. Thermal stability of Cr-doped diamond-like carbon films synthesized by cathodic arc evaporation. Thin Solid Films. 2005; 476: 258– 263

[13] Fu, R. K.Y., Mei, Y.F., Fu, M.Y., Liu, X.Y., Chu, P. K. Thermal stability of metal-doped diamond-like carbon fabricated by dual plasma deposition. Diamond & Related Materials. 2005; 14: 1489 – 1493

[14] Yang, B., Zheng, Y., Zhang, B., Wei, L. and Zhang, J. The high-temperature tribological properties of Si-DLC films. Surf. Interface Anal. 2012; 44: 1601–1605

[15] Baba, K., Hatada, R. Preparation and properties of metal-containing diamond-like carbon films by magnetron plasma source ion implantation. Surface & Coatings Technology. 2005; 196: 207– 210

[16] Yang, S., Teer, D.G. Investigation of sputtered carbon and carbon/chromium multi-layered coatings. Surface and Coatings Technology. 2000; 131; 412–416

[17] Yang, S., Li, X., Renevier, N.M., Teer, D.G. Tribological properties and wear mechanism of sputtered C/Cr coating. Surface and Coatings Technology. 2001; 142–144: 85–93

[18] Kim, M. G., Lee, K.R., Eun, K. Y. Tribological behaviour of silicon-incorporated diamond-like carbon films. Surface and Coatings Technology. 1999; 112: 204–209

[19] Pal, S. K., Jiang, J., Meletis, E. I. Effects of N-doping on the microstructure, mechanical and tribological behaviour of Cr-DLC films. Surface & Coatings Technology. 2007; 201: 7917–7923

[20] Singh, V., Jiang, J.C., Meletis, E.I. Cr-diamond like carbon nanocomposite films: Synthesis, characterization and properties. Thin Solid Films. 2005; 489: 150 – 158

[21] Dai, W., Wang A. Synthesis, characterization and properties of the DLC films with low Cr concentration doping by a hybrid linear ion beam system. Surface & Coatings Technology. 2011; 205: 2882–2886

[22] Dai, W., Ke, P., Wang A. Microstructure and property evolution of Cr-DLC films with different Cr content deposited by a hybrid beam technique. Vacuum. 2011; 85: 792–797

[23] Czyzniewski, A. Mechanical and Tribological Properties of Cr-DLC Coatings Deposited by ARC-MAG-RF PACVD Hybrid Method. Plasma Process. Polym. 2007; 4: S225–S230

[24] Hovsepian, P. Eh., Kok, Y.N., Ehiasarian, A.P., Erdemir, A., Wen, J. G., Petrov, I. Structure and tribological behaviour of nanoscale multilayer C / Cr coatings deposited by the combined steered cathodic arc/unbalanced magnetron sputtering technique. Thin Solid Films. 2004; 447–448: 7–13

[25] Kok, Y.N., Hovsepian, P.Eh., Luo Q., Lewis D. B., Wen, J. G., Petrov, I. Influence of the bias voltage on the structure and the tribological performance of nanoscale multilayer C/Cr PVD coatings. Thin Solid Films. 2005; 475: 219–226

[26] Ronkainen, H., Varjus, S., Holmberg K. Tribological performance of different DLC coatings in water-lubricated conditions. Wear. 2001; 249: 267–271

[27] Sun, J., Fu, Z., Zhang, W., Wang, C., Yue, W., Lin, S., Dai, M. Friction and wear of Cr-doped DLC films under different lubrication conditions. Vacuum. 2013; 94: 1–5

[28] Zhao F., Li H., Ji L., Wang Y., Zhou H., Chen J. Ti-DLC films with superior friction performance. Diamond & Related Materials. 2010; 19: 342–349

[29] Tsai P. C., Hwang y. F., Chiang J. Y., Chen W. J. The effects of deposition parameters on the structure and properties of titanium-containing DLC films synthesized by cathodic arc plasma evaporation. Surface & Coatings Technology. 2008; 202: 5350–5355

[30] Ronkainen H., Varjus S., Holmberg K. Friction and wear properties in dry, water- and oil-lubricated DLC against alumina and DLC against steel contacts. Wear. 1998; 222: 120–128

[31] Gharam, A. A., Lukitsch, M.J., Balogh, M.P., Irish, N., Alpas, A.T. High temperature tribological behavior of W-DLC against aluminium. Surface & Coatings Technology. 2011; 206: 1905–1912

[32] Kok, Y.N., Hovsepian, P.Eh. Resistance of nanoscale multilayer C/Cr coatings against environmental attack. Surface & Coatings Technology. 2006; 201: 3596–3605

[33] A. P. Ehiasarian, P. E. Hovsepian and W. D. Munz. US patent no. 10718435, 2005. EP 1 260 603 A2, DE 10124749, 2001.

[34] Ehiasarian A.P., Hovsepian, P. Eh., Hultman L., Helmersson U. Comparison of microstructure and mechanical properties of chromium nitride-based coatings deposited by high power impulse magnetron sputtering and by the combined steered cathodic arc/unbalanced magnetron technique. Thin Solid Films. 2004: 457: 270–277

[35] Mandal P., Ehiasarian A.P., Hovsepian, P. Eh. Lubricated sliding wear mechanism of chromium-doped graphite-like carbon coating, Tribology International. 2014; 77: 186–195

[36] Erdemir A., Donnet C. Tribology of diamond-like carbon films: recent progress and future prospects. J. Phys. D: Appl. Phys. 2006; 38: R301–R316

[37] Hutchings I. M. Tribology - Friction and Wear of Engineering Materials. Hodder Headline PLC. 1992.

[38] Oh S. J., Cook D.C., Townsend H.E. Characterization of Iron Oxides Commonly Formed as Corrosion Products on Steel. Hyperfine Interactions. 1998; 112 (1-4): 59-66

[39] Maslar J.E., Hurst W.S., Bowers W.J. Jr., Hendricks J.H., Aquino M.I., Levin I. In situ Raman spectroscopic investigation of chromium surfaces under hydrothermal condition. Applied Surface Science. 2001; 180: 102-118

[40] Frauwallner M. L., López-Linares F., Lara-Romero J., Scott C. E., Ali V., Hernández E., Pereira-Almao P. Toluene hydrogenation at low temperature using a molybdenum carbide catalyst. Applied Catalysis A: General 2011; 394: 62–70

[41] Knozinger H., Jeziorowskl H. Raman Spectra of Molybdenum Oxide Supported on the Surface of Aluminas. The Journal of Physical Chemistry. 1978; 82: 18

[42] Rout C. S., Hegde M., Rao C.N.R. H2S sensors based on tungsten oxide nanostructures. Sensors and Actuators B. 2008; 128: 488–493

[43] Chakrapani V., Thangala J., Sunkara M. K. WO3 and W2N nanowire arrays for photoelectrochemical hydrogen production. International journal of hydrogen energy. 2009; 34: 9050–9059

[44] Dieterle M. and Mestl G. Raman spectroscopy of molybdenum oxides Part II. Resonance Raman spectroscopic characterization of the molybdenum oxides Mo4O11 and MoO2. Phys. Chem. Chem. Phys. 2002; 4: 822–826

[45] Lu D. Y., Chen J., Zhou J., Deng S. Z., Xu N. S., Xu J. B. Raman spectroscopic study of oxidation and phase transition in W18O49 nanowires. J. Raman Spectrosc. 2007; 38: 176–180

[46] Chen J., Lu D., Zhang W., Xie F., Zhou J., Gong L., Liu X., Deng S., Xu N. Synthesis and Raman spectroscopic study of W20O58 nanowires. J. Phys. D: Appl. Phys. 2008; 41: 115305

[47] Mihalev M., Hardalov C., Christov C., Michailov M., Ranguelov B., Leiste H. Structural and adhesional properties of thin MoO3 films prepared by laser coating. Journal of Physics: Conference Series. 2014; 514: 012022

[48] Dieterle M., Mestl G., Jäger J., Uchida Y., Hibst H., Schlögl R. Mixed molybdenum oxide based partial oxidation catalyst 2. Combined X-ray diffraction, electron microscopy and Raman investigation of the phase stability of (MoVW)5O14-type oxides. Journal of Molecular Catalysis A: Chemical. 2001; 174 (1-2): 169-185

[49] Sharma R. K., Reddy G. B. Influence of O2 – plasma ambience and growth temperature on the oxidation of Mo-metal and volatilization of oxides. AIP Advances. 2013; 3: 092112

[50] Ferrari, A. C., Robertson, J. Interpretation of Raman spectra of disordered and amorphous carbon. Physical review B. 2000; 61: 20

[51] Tuinstra, F., Koenig, J. L. Raman Spectrum of Graphite. The Journal of Chemical Physics. 1970; 53: 3

[52] Chen X., Peng Z., Fu Z., Wu S., Yue W., Wang C. Microstructural, mechanical and tribological properties of tungsten-gradually doped diamond-like carbon films with functionally graded interlayers. Surface & Coatings Technology. 2011; 205: 3631–3638

[53] Greenwood. N. N., Earnshaw A. Chemistry of the Elements. 2nd edition - Chapter 23. Butterworth-Heinemann. 1997.

Table 1: Raman peaks of the spectra collected from the uncoated steel ball and the wear scar after sliding.

Raman peaks assigned to uncoated steel ball		Raman peaks (this work)	Raman peaks (literature)
P1		~ 100 cm^{-1} with a width of ~ 28 cm^{-1}	
P2		~ 141 cm^{-1} with a width of ~ 65 cm^{-1}	
P3		~ 218.5 cm^{-1} with a width of ~ 128 cm^{-1}	$-$
P4		~ 375 cm^{-1} with a width of ~ 253 cm^{-1}	
P5		~ 787 cm^{-1} with a width of ~ 384 cm^{-1}	
Raman peaks assigned to wear scar			
P1$^{/}$		~ 94 cm^{-1} with a width of ~ 18 cm^{-1}	
P2$^{/}$		~ 111 cm^{-1} with a width of ~ 51 cm^{-1}	$-$
P3$^{/}$		~ 177 cm^{-1} with a width of ~ 122.5 cm^{-1}	
P4$^{/}$	Fe$_2$O$_3$	~ 328 cm^{-1} with a width of ~ 311 cm^{-1}	$\sim 293 - 298$ cm^{-1} [38]
	Cr$_2$O$_3$		~ 300 cm^{-1} and ~ 350 cm^{-1} [39]
P5$^{/}$		~ 792 cm^{-1} with a width of ~ 328 cm^{-1}	$-$

Table 2: Raman peaks of the spectrum collected from the adhered debris on the counterpart after sliding.

Raman peaks assigned to	Raman peaks (this work)	Raman peaks (literature)
P1 (from uncoated steel ball)	~ 100 cm^{-1} with a width of ~ 25 cm^{-1}	–
P2 (from uncoated steel ball)	~ 137 cm^{-1} with a width of ~ 59 cm^{-1}	
P3 (from uncoated steel ball)	~ 211 cm^{-1} with a width of ~ 121.5 cm^{-1}	
MoO$_2$	~ 335 cm^{-1} with a width of ~ 215 cm^{-1}	~ 357 cm^{-1} [40]
MoO$_3$		~ 284 cm^{-1}, ~ 292 cm^{-1}, ~ 337 cm^{-1} and ~ 367 cm^{-1} [41]
WO$_3$		~ 328 cm^{-1} [42] ~ 274 cm^{-1} and ~ 315 cm^{-1} [43]
Mo$_4$O$_{11}$		~ 340 cm^{-1} [44]
W$_{18}$O$_{49}$		~ 327 cm^{-1} [45]
W$_{20}$O$_{58}$		~ 319 cm^{-1} and ~ 341 cm^{-1} [46]
Mo$_4$O$_{11}$	~ 929 cm^{-1} with a width of ~ 108 cm^{-1}	~ 907 cm^{-1} [47]
Mo$_5$O$_{14}$		~ 902 cm^{-1} [48]
Mo$_8$O$_{23}$		~ 902 cm^{-1} and ~ 958 cm^{-1} [49]

Table 3: Raman peaks of the spectrum collected from the as-deposited coating.

Raman peaks assigned to		Raman peaks (this work)	Raman peaks (literature)
P$_a$		~ 190 cm^{-1} with a width of ~ 103 cm^{-1}	-
P$_b$	Mo$_2$C	~ 342 cm^{-1} with a width of ~ 213 cm^{-1}	~ 334 cm^{-1} [40]
P$_c$		~ 652 cm^{-1} with a width of ~ 330 cm^{-1}	~ 666 cm^{-1} [40]
P$_d$		~ 100 cm^{-1} with a width of ~ 27 cm^{-1}	-
P$_e$		~ 131.5 cm^{-1} with a width of ~ 54 cm^{-1}	

Table 4: Raman peaks of the spectrum collected within the wear track after sliding.

Raman peaks assigned to		Raman peaks (this work)	Raman peaks (literature)
$P_a^{/}$		~ 173 cm^{-1} with a width of ~ 100 cm^{-1}	-
$P_b^{/}$	Mo$_2$C (from as-deposited coating)	~ 320 cm^{-1} with a width of ~ 226 cm^{-1}	~334 cm^{-1} [40]
	WO$_3$		~315 cm^{-1} [43] ~328 cm^{-1} [42]
	W$_{18}$O$_{49}$		~327 cm^{-1} [45]
	W$_{20}$O$_{58}$		~319 cm^{-1} and ~341 cm^{-1} [46]
$P_c^{/}$	Mo$_2$C (from as-deposited coating)	~ 644 cm^{-1} with a width of ~ 383 cm^{-1}	~666 cm^{-1} [40]
	MoO$_2$		~640 cm^{-1} and ~666 cm^{-1} [40]
	MoO$_3$		~667 cm^{-1} [41]
	Mo$_8$O$_{23}$		~658 cm^{-1} [49]
WC		~ 942 cm^{-1} with a width of ~150 cm^{-1}	~960 cm^{-1} [52]
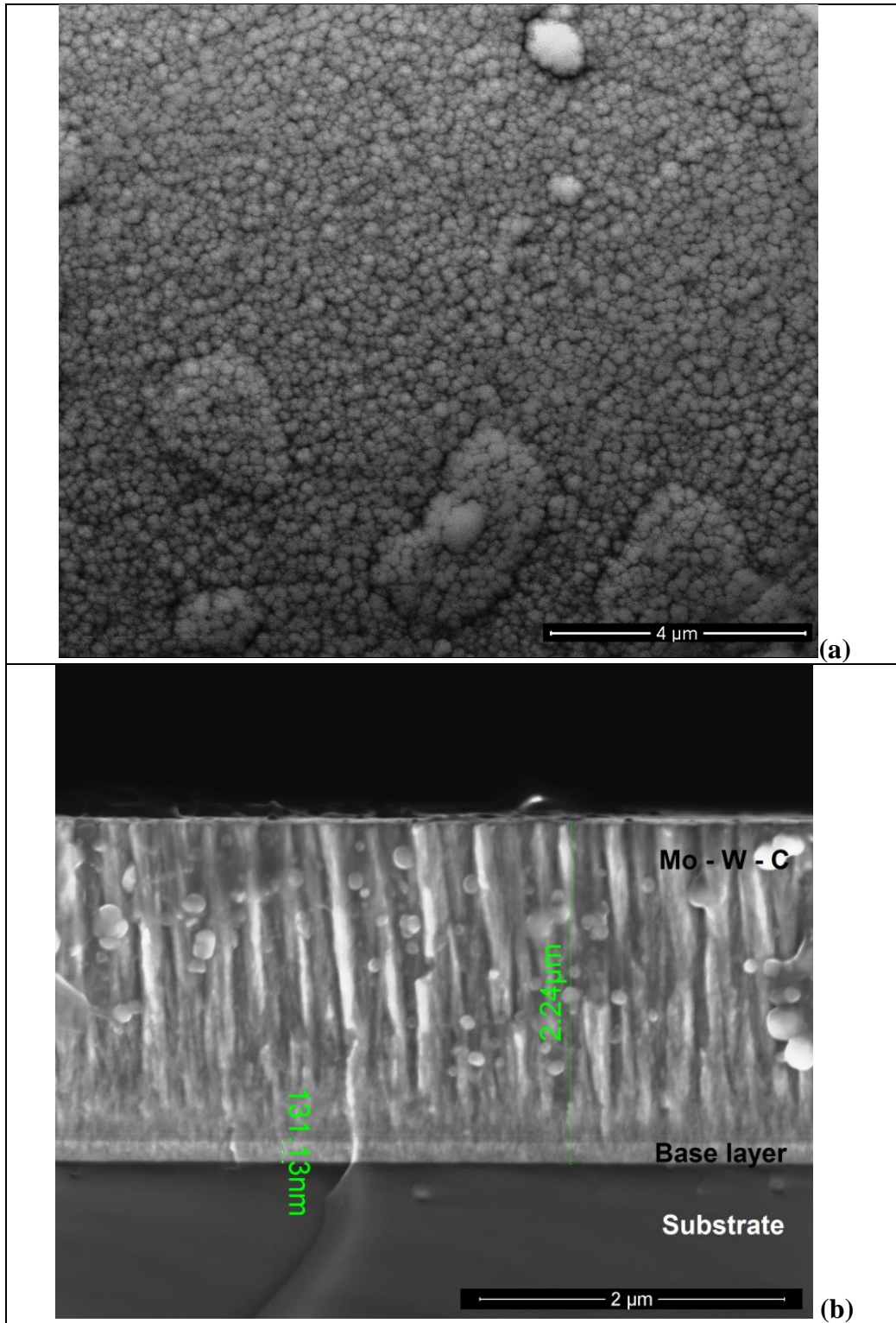
Figure 1: (a) Surface morphology and (b) cross-sectional SEM image of as-deposited Mo−W−C coating
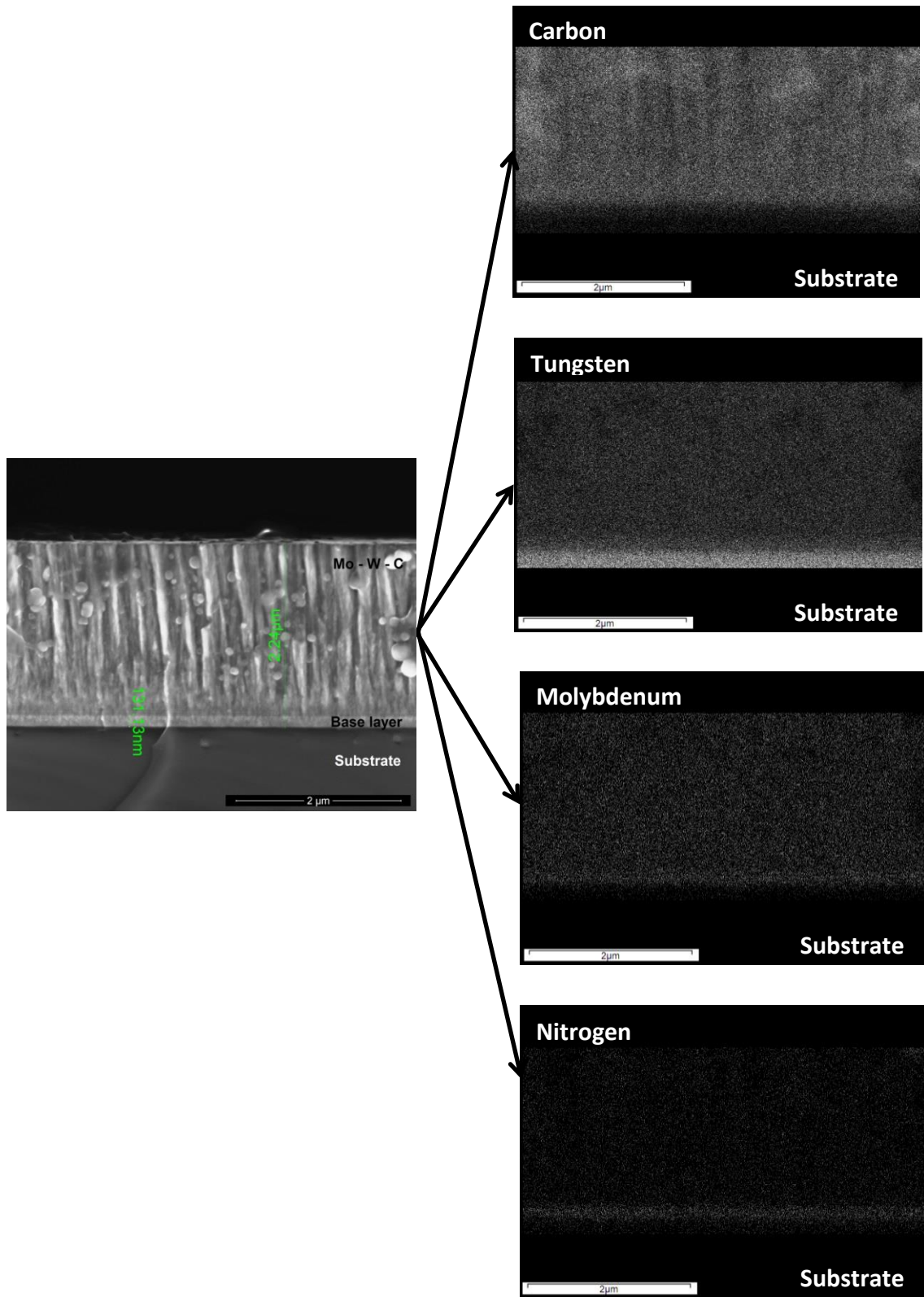
Figure 2: X-ray mapping of elements on the fracture cross-section of as-deposited Mo−W−C coating
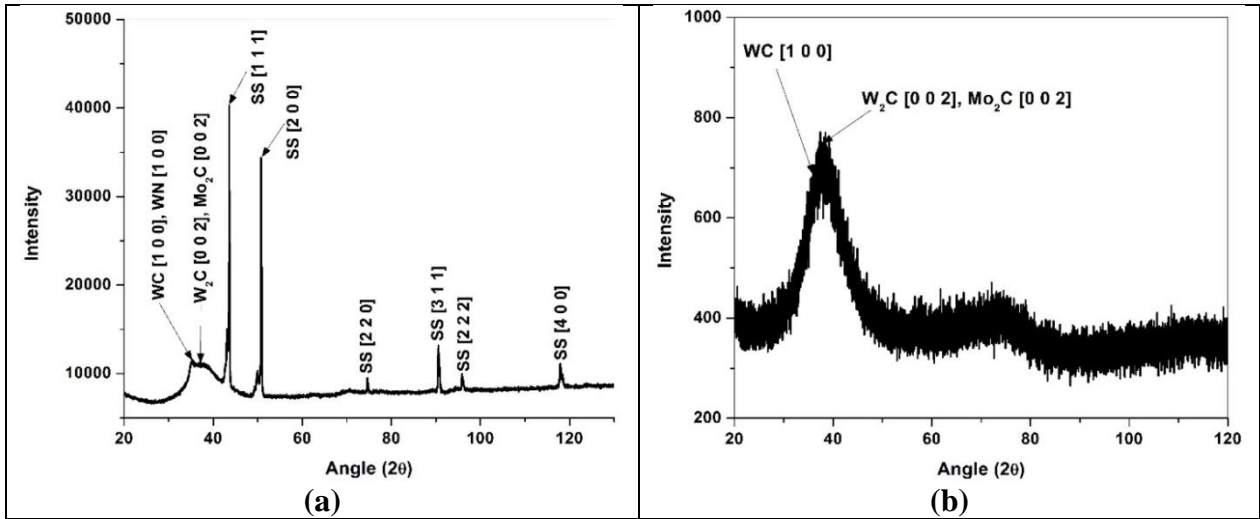
Figure 3: XRD patterns of as-deposited Mo−W−C coating using (a) Bragg-Brentano and (b) glancing angle geometry
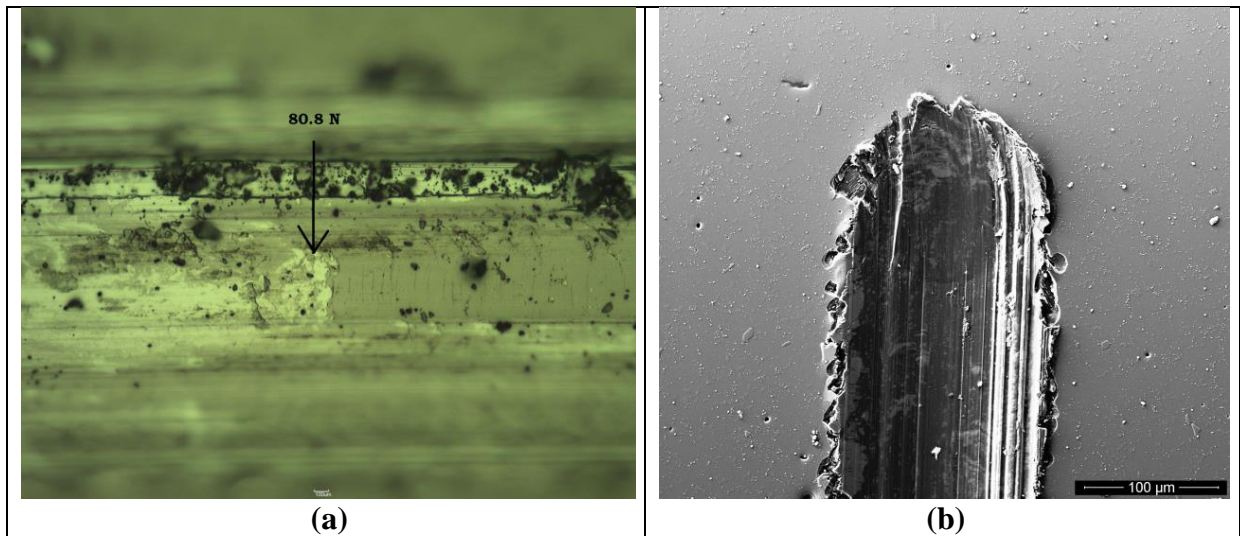
Figure 4: Adhesion strength of Mo−W−C coating showing (a) critical load (L$_c$) and (b) the scratch track end for 100 N applied load
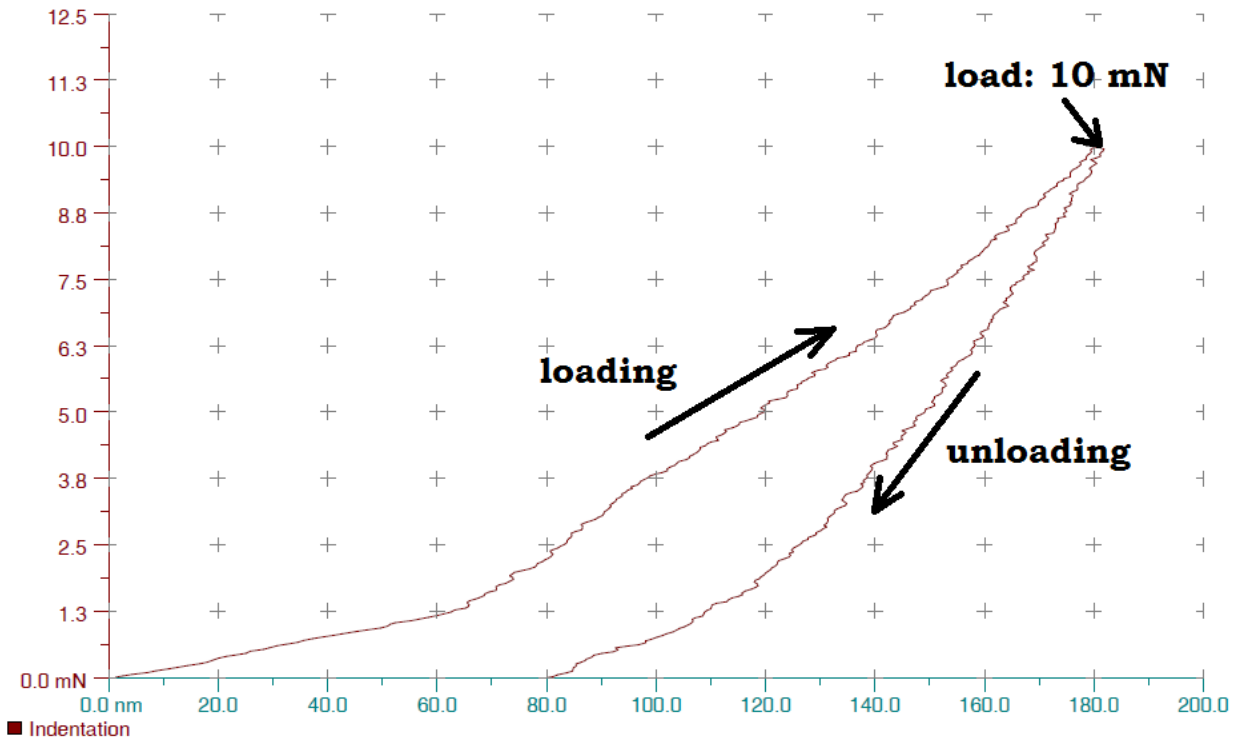
Figure 5: A typical characteristic loading-unloading curve of Mo−W−C coating
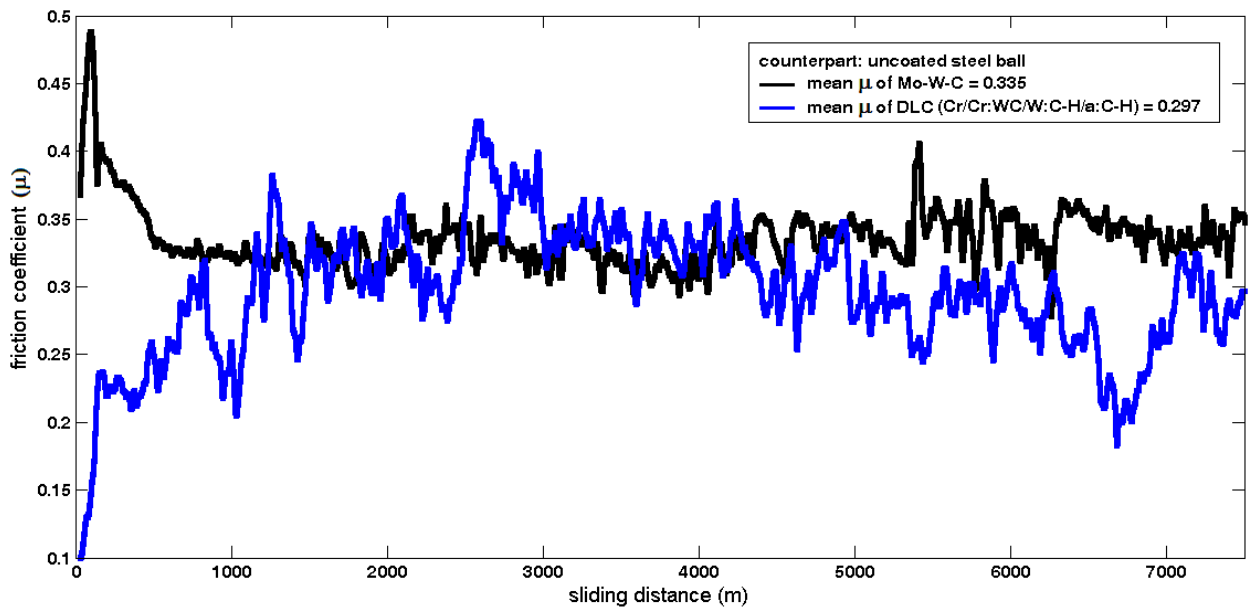
Figure 6: Friction behaviour of Mo−W−C and state-of-the-art DLC coatings at ambient condition
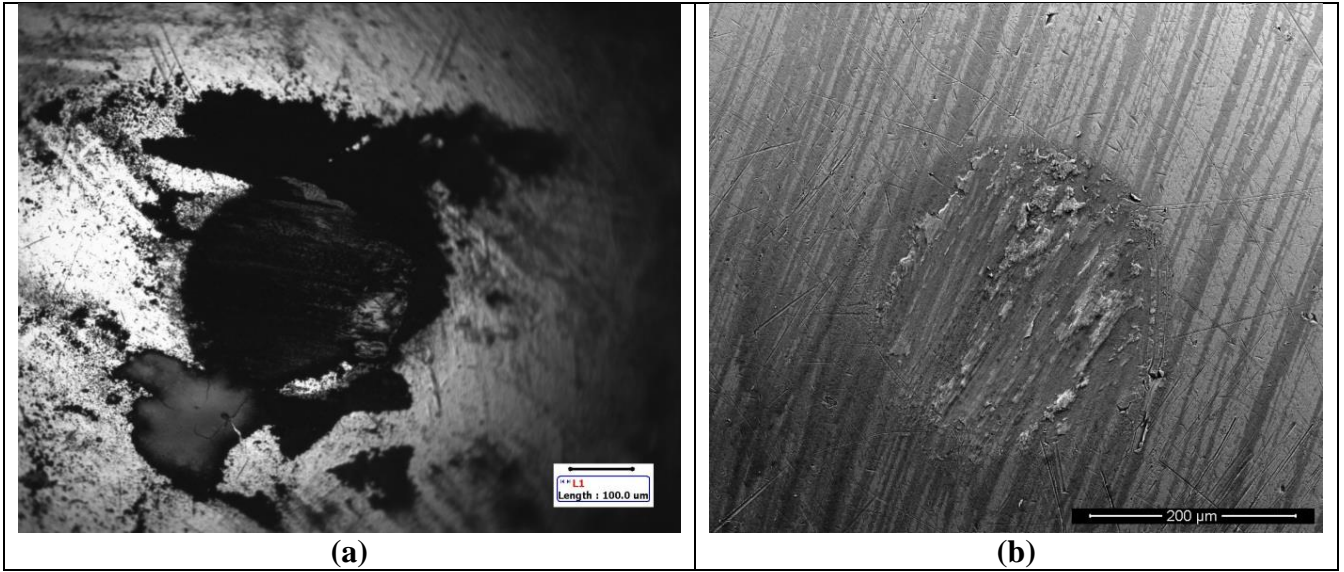
Figure 7: (a) Transfer layer formed on the uncoated steel ball and (b) debris strongly adhered

to the counterpart surface after dry sliding
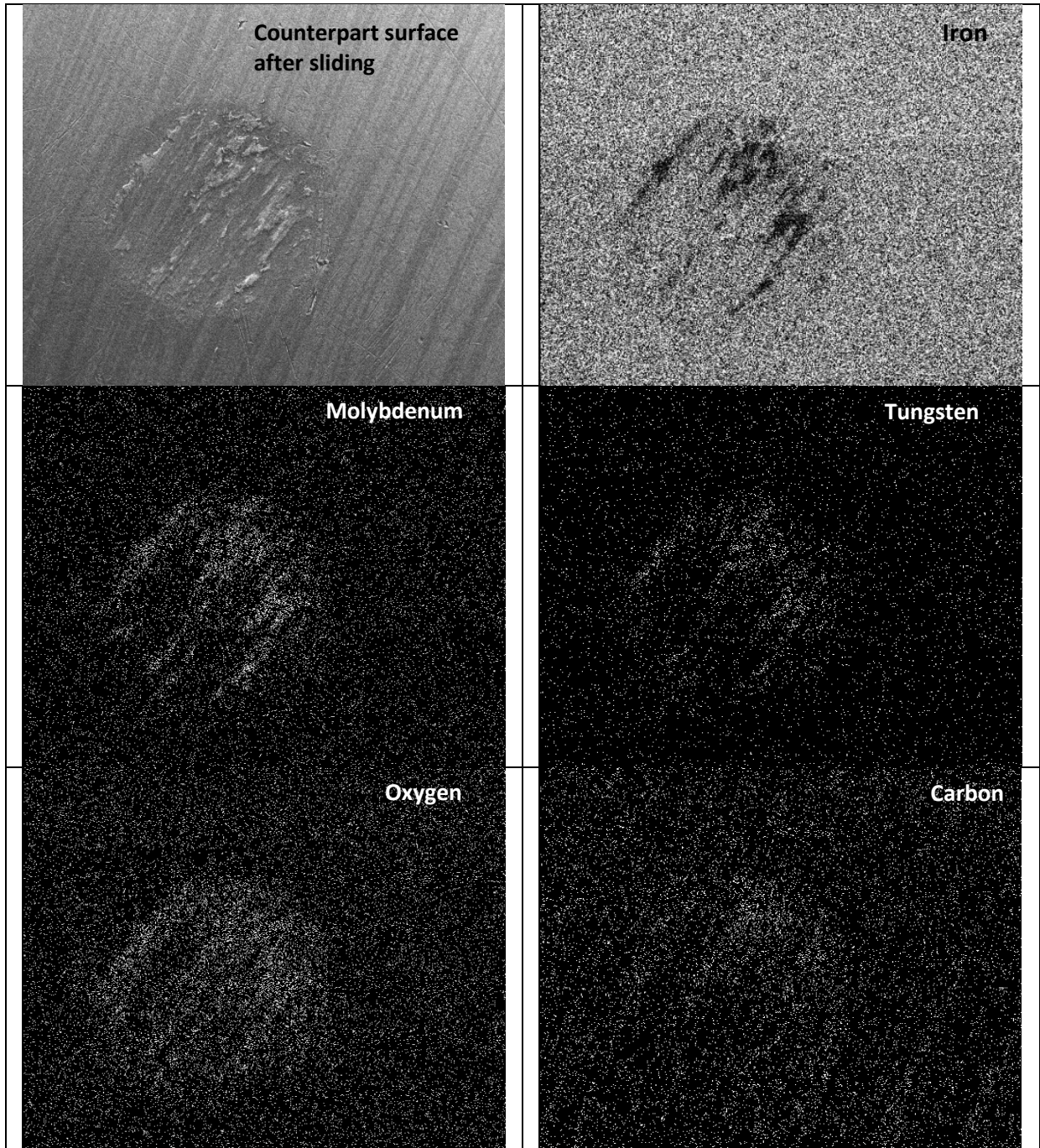
Figure 8: X-ray mapping of the debris adhered to the counterpart surface after dry sliding
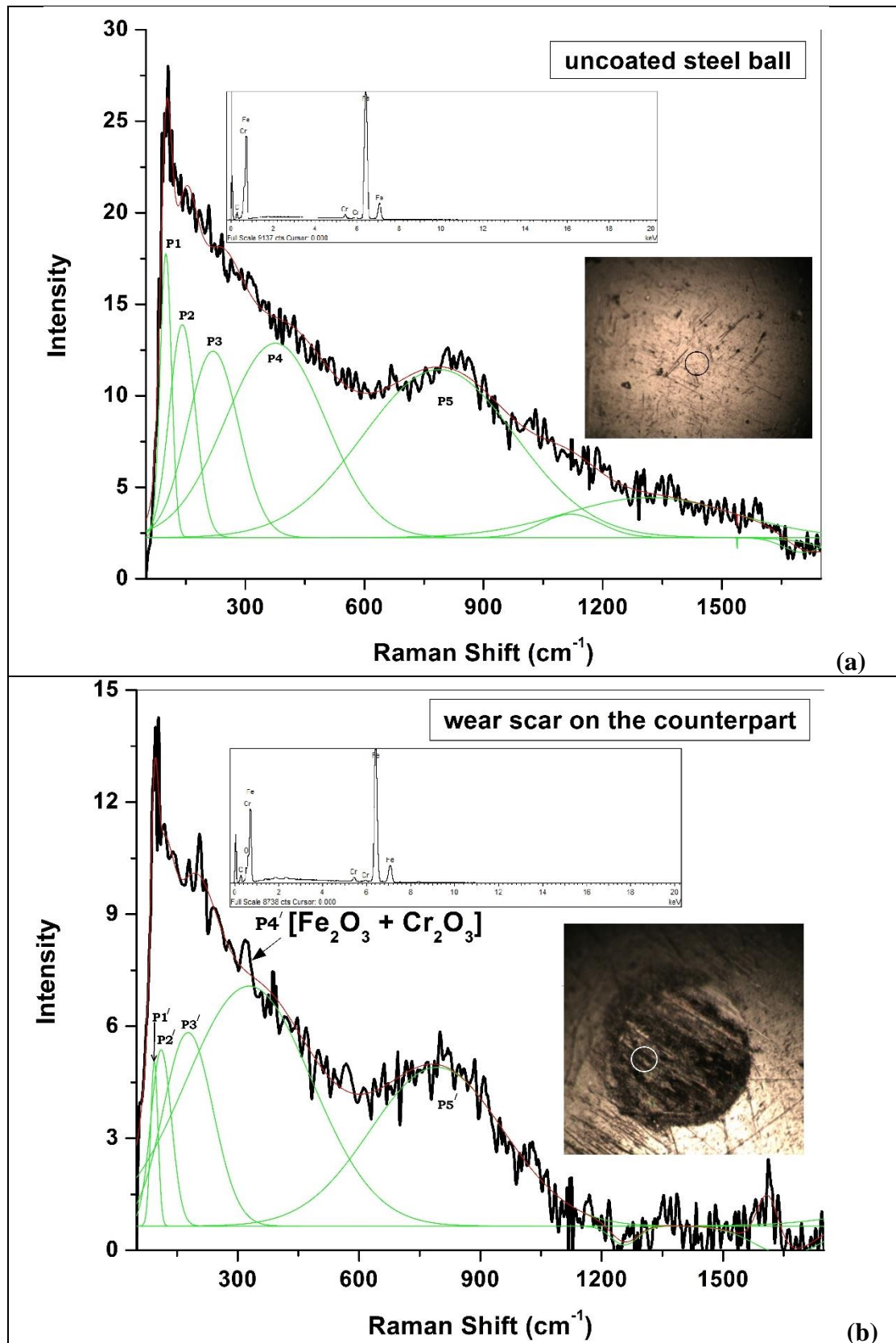
Figure 9: Raman spectra collected from the (a) uncoated steel ball and (b) wear scar on the counterpart after dry sliding
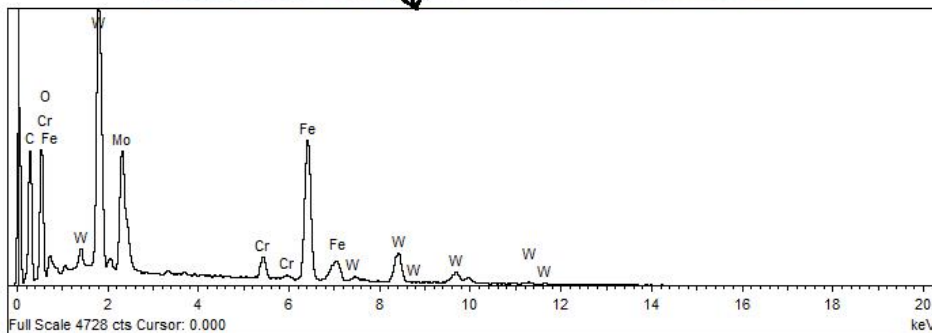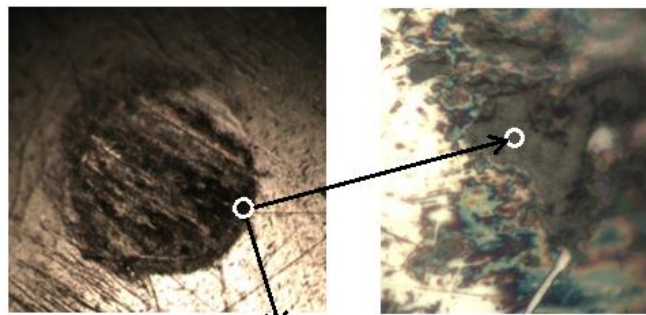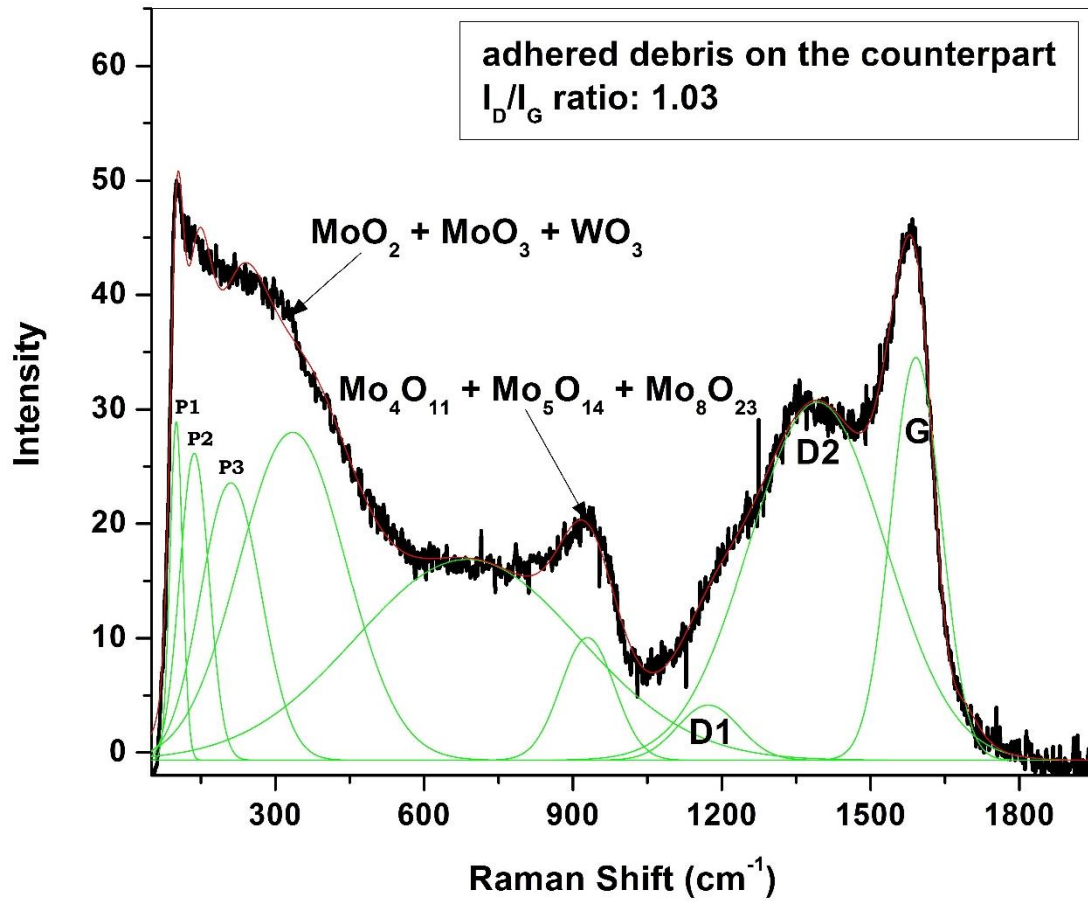
Figure 10: Raman spectrum collected from the debris adhered to the counterpart surface after dry sliding
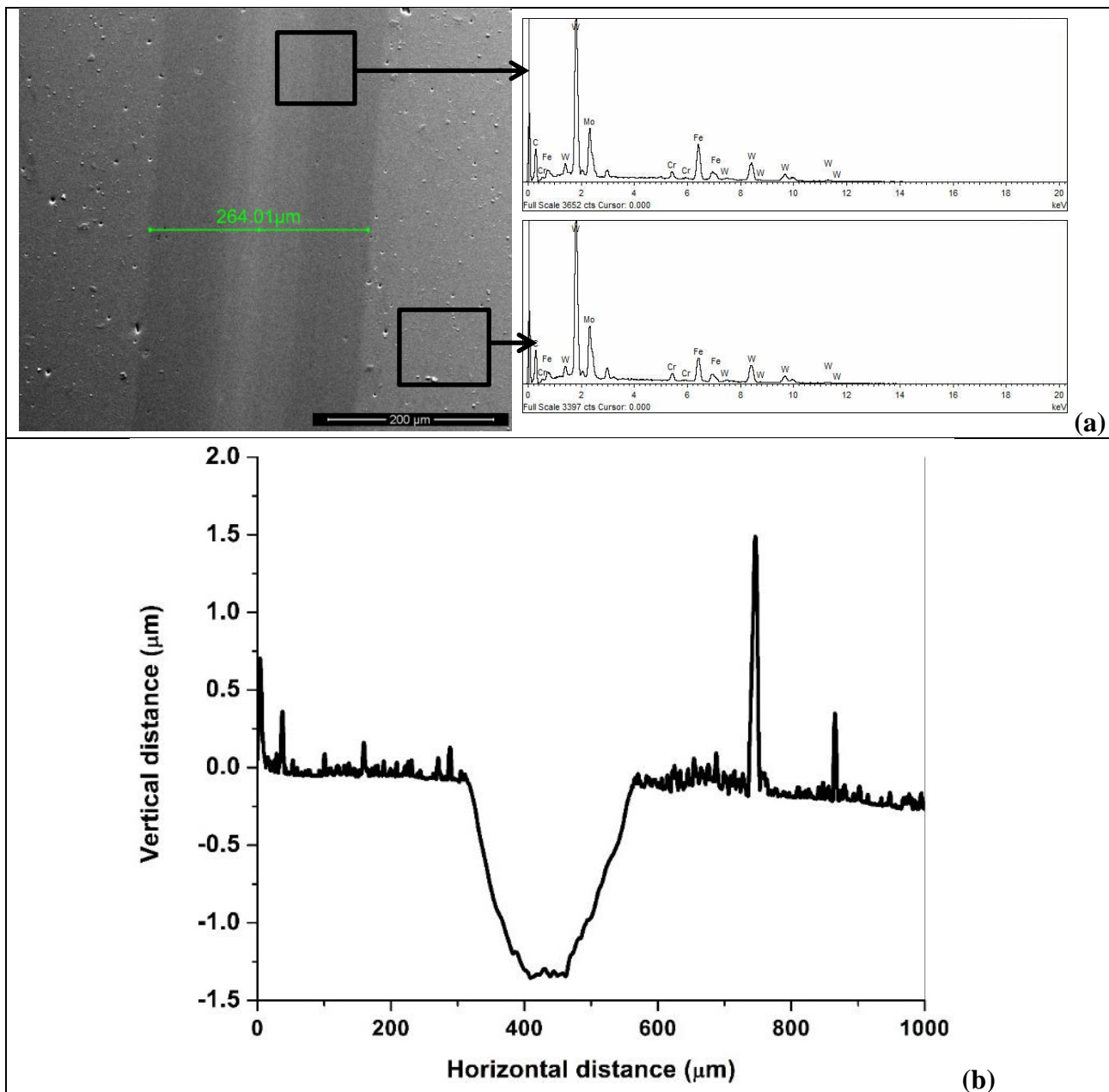
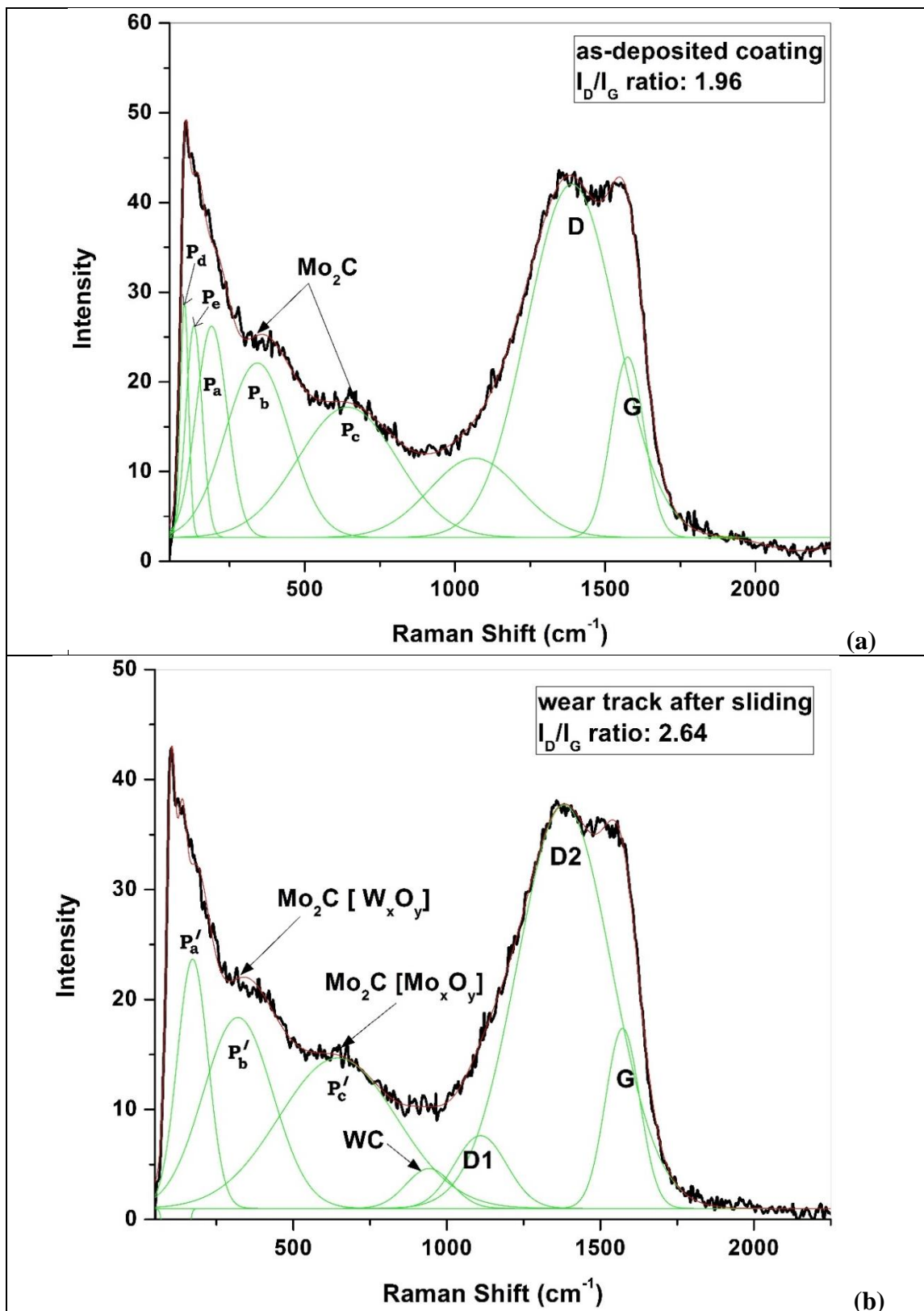Figure 11: (a) Wear track after dry sliding and (b) profile of the wear track

Figure 12: Raman spectra collected from (a) as-deposited Mo−W−C coating and (b) within the wear track after dry sliding